

A Terrestrial Planet in a ~ 1 AU Orbit Around One Member of a ~ 15 AU Binary

A. Gould,¹ A. Udalski², I.-G. Shin³, I. Porritt⁴, J. Skowron²,
C. Han^{3,5}, J. C. Yee^{1,6}, S. Kozłowski², J.-Y. Choi³,

and

R. Poleski^{1,2}, Ł. Wyrzykowski^{2,7}, K. Ulaczyk², P. Pietrukowicz², P. Mróz²,
M.K. Szymański², M. Kubiak², I. Soszyński², G. Pietrzyński^{1,8}

(OGLE Team),

B.S. Gaudi¹, G.W. Christie⁹, J. Drummond¹⁰, J. McCormick¹¹,

T. Natusch^{10,12}, H. Ngan¹⁰, T.-G. Tan¹³, M. Albrow¹⁴,

D.L. DePoy¹⁵, K.-H. Hwang³, Y.K. Jung³, C.-U. Lee¹⁶,

H. Park³, R.W. Pogge¹,

(μ FUN Team),

F. Abe¹⁷, D. P. Bennett¹⁸, I. A. Bond¹⁹, C. S. Botzler²⁰, M. Freeman²⁰,

A. Fukui²¹, D. Fukunaga¹⁷, Y. Itow¹⁷, N. Koshimoto²², P. Larsen^{20,29},

C. H. Ling¹⁹, K. Masuda¹⁷, Y. Matsubara¹⁷, Y. Muraki¹⁷, S. Namba²²,

K. Ohnishi²³, L. Philpott³⁰, N. J. Rattenbury²⁰, To. Saito²⁴, D. J. Sullivan²⁵,

T. Sumi²², D. Suzuki²², P. J. Tristram²⁶, N. Tsurumi¹⁷, K. Wada²²,

N. Yamai²⁷, P. C. M. Yock²⁰, A. Yonehara²⁷,

(MOA Team),

Y. Shvartzvald²⁸, D. Maoz²⁸, S. Kaspi²⁸, M. Friedmann²⁸,

(Wise Team),

¹Department of Astronomy, Ohio State University, 140 W. 18th Ave., Columbus, OH 43210, USA

²Warsaw University Observatory, Al. Ujazdowskie 4, 00-478 Warszawa, Poland

³Department of Physics, Chungbuk National University, Cheongju 371-763, Republic of Korea

⁴Turitea Observatory, Palmerston North, New Zealand

⁵Corresponding Author

⁶Harvard-Smithsonian Center for Astrophysics, 60 Garden St., Cambridge, MA 02138, USA

- ⁷Institute of Astronomy, University of Cambridge, Madingley Road, Cambridge CB3 0HA, UK
- ⁸Universidad de Concepción, Departamento de Astronomía, Casilla 160–C, Concepción, Chile
- ⁹Auckland Observatory, Auckland, New Zealand
- ¹⁰Possum Observatory, Patutahi, New Zealand
- ¹¹Farm Cove Observatory, Centre for Backyard Astrophysics, Pakuranga, Auckland, New Zealand
- ¹²AUT University, Auckland, New Zealand
- ¹³Perth Exoplanet Survey Telescope, Perth, Australia
- ¹⁴Dept. of Physics and Astronomy, University of Canterbury, Private Bag 4800, Christchurch, New Zealand
- ¹⁵Dept. of Physics and Astronomy, Texas A&M University, College Station, Texas 77843-4242, USA
- ¹⁶Korea Astronomy and Space Science Institute, Daejeon 305-348, Republic of Korea
- ¹⁷Solar-Terrestrial Environment Laboratory, Nagoya University, Nagoya, 464-8601, Japan
- ¹⁸University of Notre Dame, Department of Physics, 225 Nieuwland Science Hall, Notre Dame, IN 46556-5670, USA
- ¹⁹Institute of Information and Mathematical Sciences, Massey University, Private Bag 102-904, North Shore Mail Centre, Auckland, New Zealand
- ²⁰Department of Physics, University of Auckland, Private Bag 92-019, Auckland 1001, New Zealand
- ²¹Okayama Astrophysical Observatory, National Astronomical Observatory of Japan, Asakuchi, Okayama 719-0232, Japan
- ²²Department of Earth and Space Science, Osaka University, Osaka 560-0043, Japan
- ²³Nagano National College of Technology, Nagano 381-8550, Japan
- ²⁴Tokyo Metropolitan College of Aeronautics, Tokyo 116-8523, Japan
- ²⁵School of Chemical and Physical Sciences, Victoria University, Wellington, New Zealand
- ²⁶Mt. John University Observatory, P.O. Box 56, Lake Tekapo 8770, New Zealand
- ²⁷Department of Physics, Faculty of Science, Kyoto Sangyo University, 603-8555, Kyoto, Japan
- ²⁸School of Physics and Astronomy, Tel-Aviv University, Tel-Aviv 69978, Israel
- ²⁹Institute of Astronomy, University of Cambridge, Madingley Road, Cambridge CB3 0HA, UK
- ³⁰Department of Earth, Ocean and Atmospheric Sciences, The University of British Columbia, Vancouver, British Columbia, V6T 1Z4, Canada

We detect a cold, terrestrial planet in a binary-star system using gravitational microlensing. The planet has low mass (2 Earth masses) and lies projected at $a_{\perp,ph} \simeq 0.8$ astronomical units (AU) from its host star, similar to the Earth-Sun distance. However, the planet temperature is much lower, $T < 60$ Kelvin, because the host star is only 0.10–0.15 solar masses and therefore more than

400 times less luminous than the Sun. The host is itself orbiting a slightly more massive companion with projected separation $a_{\perp, ch} = 10\text{--}15$ AU. Straight-forward modification of current microlensing search strategies could increase their sensitivity to planets in binary systems. With more detections, such binary-star/planetary systems could place constraints on models of planet formation and evolution. This detection is consistent with such systems being very common.

Although at least half of all stars are in binary or multiple systems, the overwhelming majority of detected exoplanets orbit single stars, or at least stars whose companions have not been detected or are so far from the planet’s host as to be physically irrelevant. Because binary stars are so common, theories of planet formation and orbital evolution should be strongly constrained by the observed frequency and parameter distributions of planets in these systems. For example, the presence of a relatively near companion might truncate or disrupt the protoplanetary disk that is thought to be the planet birthplace. Exploring planets in binary systems is therefore an important frontier.

Microlensing is complementary to other planet-finding techniques in terms of sensitivity as functions of planet-host separation, host mass, planet mass, and planet-host position within our Galaxy. The basic scale of microlensing phenomena is set by the Einstein radius (θ_E)

$$\theta_E \equiv \sqrt{\kappa M \pi_{\text{rel}}}; \quad \kappa \equiv \frac{4G}{c^2 \text{AU}} \simeq 8.1 \frac{\text{mas}}{M_{\odot}}, \quad (1)$$

where M is the lens mass, $\pi_{\text{rel}} = \text{AU}(D_L^{-1} - D_S^{-1})$ is the lens-source relative parallax, and D_L and D_S are the distances to the lens and source, respectively. If two stars are perfectly aligned on the sky, then the gravity of the one in front (“lens”) bends the light from the one in back (“source”) into an annulus (“Einstein ring”) of radius θ_E and width twice θ_* , where θ_* is the source angular radius. If the lens-source separation $\Delta\theta_{LS}$ is nonzero but still $\Delta\theta_{LS} \lesssim \theta_E$, then

the source light is broken up into two images, one inside and the other outside the Einstein ring. The two images are separated by $\theta_E \sim \mathcal{O}(\text{mas})$ (10^{-3} arcseconds) and so are not resolvable with current telescopes. However, the combined area of the images is larger than the source and so appears brighter by the magnification A , which scales very nearly as $(\Delta\theta_{LS}/\theta_E)^{-1} \equiv u^{-1}$ for $u \lesssim 0.5$. Hence, as the lens passes by the projected position of the source, the magnification increases and then decreases, creating a “microlensing event”. Currently, over 2000 such events are discovered each year. If the lens has a planet, and one of the two images passes near this planet, its gravity further deflects the light, changing the lightcurve and thereby betraying its presence. Planet sensitivity peaks over the range $0.6\theta_E \lesssim a_\perp/D_L \lesssim 1.6\theta_E$, which corresponds to a planet-host physical separation a_\perp

$$a_\perp \sim r_E \equiv D_L \theta_E \sim 3.5 \text{ AU} \sqrt{\frac{M}{M_\odot}} \quad (2)$$

for typical event parameters. Because this is a 2-dimensional (2D) projection of a 3-D elliptical orbit, with semi-major axis a , the semi-major axis is typically larger by $a/a_\perp \sim \sqrt{3/2}$, i.e. $a \sim 4.3 \text{ AU}$ for a solar-mass host. By contrast, the “snow line”, outside of which ices can condense and so promote the growth of giant planets, is 2.7 AU in the solar system and is generally believed to increase monotonically with host mass (e.g. (2)). Hence, microlensing probes planets in the cold outer regions, far from their host stars. By contrast, the radial velocity (RV) and transit techniques are most sensitive to planets much closer to hosts, and imaging is sensitive to planets much further out. Because microlensing does not depend on host (or planet) light, it is sensitive to low-luminosity (even non-luminous) hosts and to systems that are many kiloparsecs (kpc) away. Finally, in sharp contrast to all other methods, the amplitude of the microlensing signal does not necessarily decline as the planet mass decreases. This does not mean that microlensing is equally sensitive to all planet masses: the linear extent of the planetary caustic (closed curve of formally infinite magnification) declines as \sqrt{q} , where $q = m_p/M$,

Name	Location	Diam.(m)	Filter
OGLE	Chile	1.3	I
MOA	New Zeal.	1.8	RI
Wise	Israel	1.0	I
Auckland	New Zeal.	0.40	R
CTIO-SMARTS	Chile	1.3	I
Farm Cove	New Zeal.	0.36	N
PEST	West Aus.	0.30	N
Possum	New Zeal.	0.36	N
Turitea	New Zeal.	0.36	R

Table 1. Observatories.

which reduces both the probability and duration of perturbation by \sqrt{q} . However, when these perturbations occur, they can be robustly detected (see review by Gaudi (3)).

Microlensing event OGLE-2013-BLG-0341 was detected by the Optical Gravitational Lens Experiment¹ (OGLE, Chile) (4) and was also observed in survey mode by two other surveys, Microlensing Observations in Astrophysics² (MOA, New Zealand) (5, 6) and Wise³ (7) (Israel). It was intensively observed in followup mode by six Microlensing Follow Up Network⁴ (μ FUN) observatories. See Table 1.

The precise extraction of all parameters requires computationally intensive modeling (see Supplements (8)), but the characteristics relevant to the main scientific implications of this discovery can mostly be derived from inspection of the light curve (Fig. 1). There are three main features, a double-horned peak lasting ~ 1 day centered at $t \sim 6406.5$ day, an extended, very shallow “bump” at $t \sim 6100$ day, and a very short “dip” at $t \sim 6394$ day. The first two are due to the binary and the last is due to the planet. Such features have been seen and analyzed

¹<http://ogle.astrouw.edu.pl/ogle4/ews/ews.html/>

²<https://it019909.massey.ac.nz/moa/>

³<http://wise-obs.tau.ac.il/~wingspan/>

⁴<http://www.astronomy.ohio-state.edu/~microfun/>

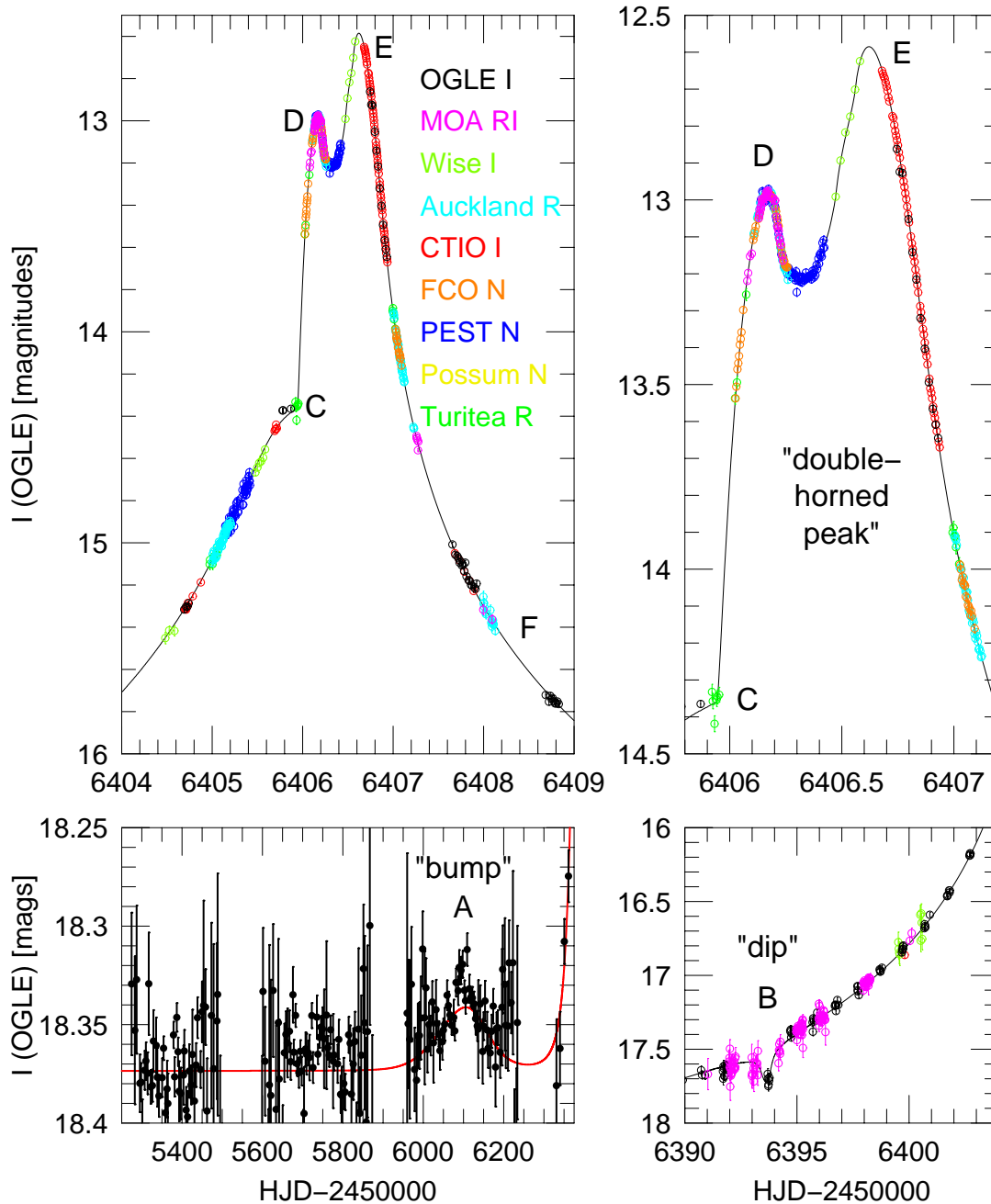


Figure 1: OGLE-2013-BLG-0341 lightcurve. Upper panels: lightcurve features (C through F), induced by main caustic due to binary, are seen as source passes close to planet host. The entrance has a sharp break (C) indicating a caustic crossing, while the exit does not (EF), indicating a cusp exit. Lower-left: low amplitude “bump” (A) due to sources passage relatively far from binary companion to host, ~ 300 days earlier. Lower-right: “dip” (B) due to planet “annihilating” one of the the two main images of the source.

previously in many planetary and binary microlensing events; the difference in this case is that 1) they appear together, and 2) there is a subtle interplay between them. The duration of the principal peak is ~ 65 times shorter than the Einstein diameter crossing time $2t_E$, where $t_E \equiv \theta_E/\mu_{\text{rel}} \sim 33$ days and μ_{rel} is the lens-source relative angular speed. This peak is therefore due to a very small central caustic, which could in principle be due either to a planet near the Einstein ring, or to a companion star that is far from it. The sharp beginning ($t \sim 6406.0$ day) and smooth end ($t > 6407$ day) imply fold-caustic entrance and cusp exit (Fig. 2). This morphology is consistent only with a binary lens. Although the binary companion could be, in theory, either very far inside (“close”) or very far outside (“wide”) the Einstein ring, the early bump at $t \sim 6100$ day confirms the latter interpretation: this bump was generated by the source passing moderately close to the companion a year earlier (Fig. 2). Finally, the small dip at $t \sim 6394$ day can only be caused by a planet that is inside the Einstein ring. Recall that the principal lens creates two images, which are at extrema of the time-delay surface (Fermat’s Principle). The outside image is at a minimum of this surface, and the inside image is at a saddle point. A planet sitting at exactly this saddle point will effectively annihilate the image, causing a dip. To generate only a dip and no neighboring bumps, the source must have “threaded” the planetary-caustic structure as it headed toward the central caustic (Fig. 2). The half-crossing time of the dip is $t_{\text{dip}} \sim 0.25$ day. Because the planetary caustic size scales as $(t_{\text{dip}}/t_E) \sim q^{1/2}$, the planet is $q \sim 0.6 \times 10^{-4}$ times less massive than its host. From the fact that the interval between the planetary and binary caustics is $\sim 0.4 t_E$, we calculate that the planet-host separation (normalized to the Einstein radius) is $s_2 \sim 1 - 0.4/2 = 0.8$ from the center of magnification of the system (which in this binary system is very close to the host).

The next step is to transform the dimensionless separations into angles by measuring θ_E , using the source size θ_* as a “ruler” (9). From its measured color (and thus, since stars are approximate black bodies, surface brightness, S) and flux F , we determine $\theta_* = \sqrt{F/\pi S} = 2.9 \mu\text{as}$ (8).

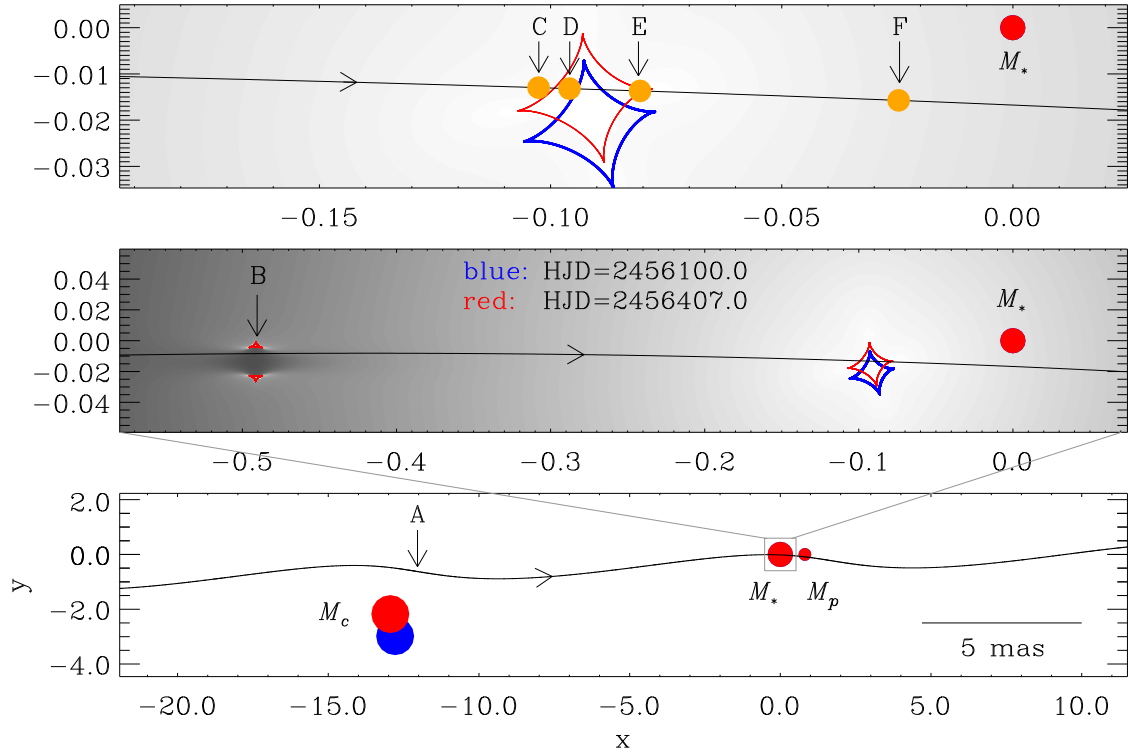


Figure 2: Geometry of OGLE-2013-BLG-0341 “Wide minus” solution. This includes locations of the host (M_*), planet (M_p), and companion (M_c), and of the caustics (closed curves of formally infinite magnification) that induce strong perturbations in the lightcurve. Source position is shown at six key times (ABCDEF) corresponding to lightcurve features in Fig. 1. Middle panel: Zoom of planetary caustic (left) and central caustic (right) giving rise to “dip” and main peak seen in Fig. 1. Central caustic and lens positions are shown at two different epochs (“A” and “E”) separated by ~ 300 days during which it changed its shape and orientation due to binary orbital motion as described in Supplements. Upper panel: Further zoom showing source (yellow) to scale. Blue and red caustics and circles indicate lens geometries at times of “bump” (A) and main peak (D), respectively. One unit on x -axis corresponds to $t_E = 33$ days in time.

Comparing the caustic rise time (6405.97–6406.17) to the standard mathematical form (steep, then rounded rise totaling 1.7 source-radius crossing times, (10)), and for simplicity ignoring that this entrance is at an angle, we can estimate a source crossing time of $t_* \sim 0.12$ days. The resulting Einstein radius is $\theta_E = (t_E/t_*)\theta_* \sim 0.8$ mas.

The final step is to measure the distance using the “microlens parallax”, $\pi_E \equiv \pi_{\text{rel}}/\theta_E$. This quantifies the amplitude of lens-source relative motion due to reflex motion of Earth’s orbit (scaled to the Einstein radius) and therefore the amplitude of the lightcurve deviations due to this effect (see (11), Fig. 1 for a didactic explanation). The impact of this effect on the lightcurve is easily seen (if not quantified) in the residuals to models with and without parallax (see Fig. 3). There is a well known degeneracy in parallax solutions (labeled “+/-”), depending on which side of the projected position of Earth the lens passes relative to the source (12), and we show (8) that this degeneracy cannot be broken in this case⁵. Thus, we find $\pi_E = 1.0$ or $\pi_E = 0.8$. Then from the definitions of θ_E and π_E , we obtain $\pi_{\text{rel}} = \theta_E\pi_E$ and $M = \theta_E/\kappa\pi_E$ and have calculated the relevant physical parameters that are derived from each of the two solutions (Table 2).

In either case, the planet has mass $m_p \sim 2$ Earth masses (M_\oplus) and the host is a late M dwarf, with another, slightly more massive, M dwarf as a companion lying at a projected separation of 10 or 14 AU. The entire system lies ~ 1 kpc from the Sun. Simulations of microlensing with realistic planetary systems that include eccentricity and inclination (13) confirm the naive expectation that these projected separations are good proxies for the semi-major axis (after upward adjustment by $\sqrt{3/2}$ to correct for projection effects). Indeed, the relation between a and a_\perp is very similar to the relation between m and $m \sin i$ for RV detections. Hence, as with RV masses, this proxy can fail badly in rare individual cases.

What are the implications? First, while we cannot reliably estimate the frequency of such systems, we can ask the simpler question: if all stars were in such binary/terrestrial-planet

⁵We also include in the model orbital motion of the binary about its center of mass. These effects are discussed in detail in the Supplement, but are too subtle to detect by eye from the lightcurve.

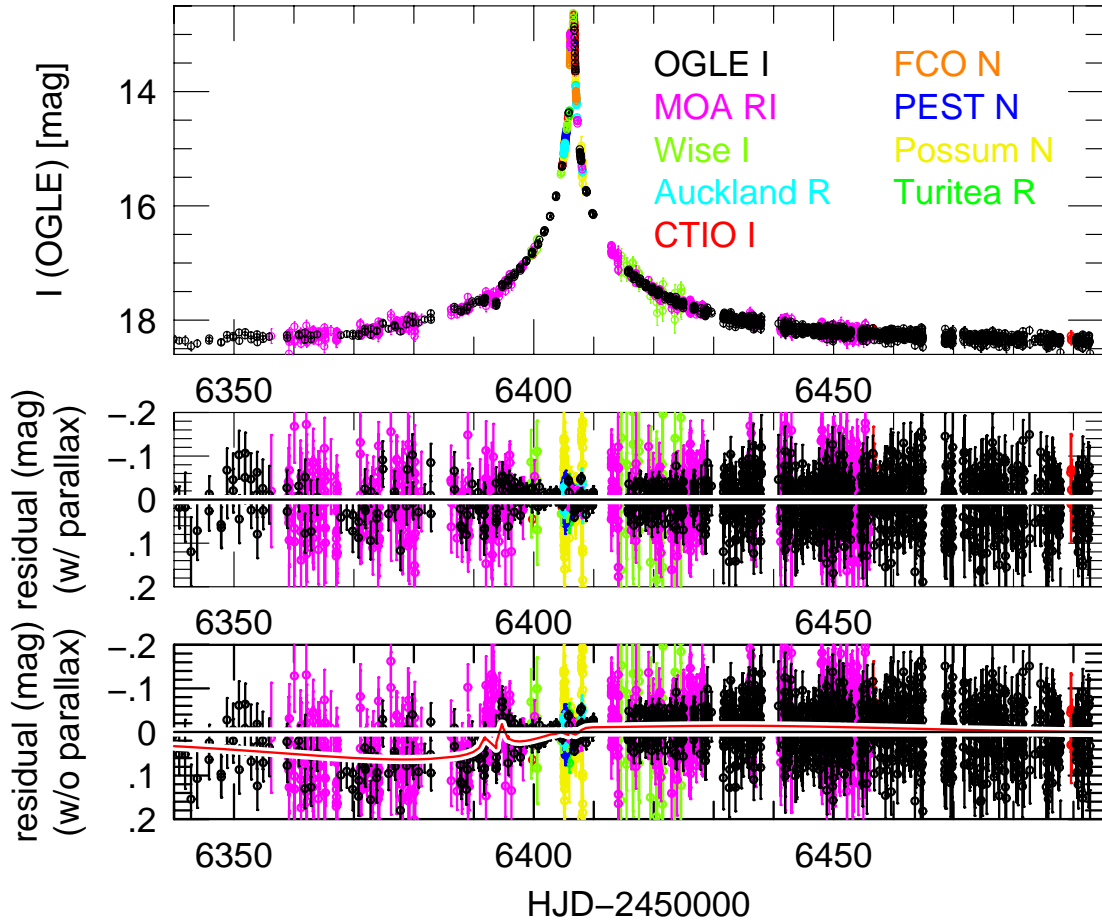


Figure 3: Full OGLE-2013-BLG-0341 lightcurve (top) and residuals from “Wide minus” model with (middle) and without (bottom) including the parallax effect. Parallax is strongly detected, $\Delta\chi^2 = 730$. Silhouetted black and red curves indicate zero and difference between parallax and no-parallax models, respectively. In contrast to all other crucial lightcurve parameters, the parallax effect is not directly visible in the lightcurve, but only in the residuals. However, as explained in Supplements, an experienced modeler can “read off” from these residuals that $\pi_E \gtrsim 0.7$.

Parameter	Unit	Wide(+)	Wide(-)
M_{total}	M_{\odot}	0.2336	0.3207
		0.0182	0.0284
M_{host}	M_{\odot}	0.1127	0.1452
		0.0089	0.0135
M_{planet}	M_{\oplus}	1.66	2.32
		0.18	0.27
$M_{\text{companion}}$	M_{\odot}	0.1209	0.1755
		0.0094	0.0155
Distance	kpc	0.911	1.161
		0.070	0.093
$a_{\perp,ph}$	AU	0.702	0.883
		0.022	0.043
$a_{\perp,ch}$	AU	10.536	14.013
		0.318	0.617

Table 2. Physical Parameters of the binary + planet models. Masses, Distances, and projected separations for binary+planet system in the two models that are consistent with the microlensing data.

systems, how many should have been detected? The detection required 1) a transit of the source by both the planetary ($p \sim 6 \times 10^{-3}$) and central caustics ($p \sim 7 \times 10^{-2}$) and 2) relatively high-cadence data on a relatively bright star $I_S < 18.5$ to ensure sufficient signal-to-noise ratio to detect the dip. Therefore, if all $I < 18.5$ stars that undergo microlensing events had such planets, we would detect $\sim 0.04\%$ of them. During the three years that OGLE-IV has issued alerts, it detected a total of $\sim 10^3$ of $I_S < 18.5$ events in its high-cadence fields, which implies an expectation of 0.4 such planets. This would be compatible with survey results showing that Earths and super-Earths are the most common type of planet orbiting stars with a wide range of masses (14–18) and with predictions from microlensing based on more massive planets orbiting low-mass stars (19).

Second, this result shows that terrestrial planets can exist relatively far (~ 1 AU) from their hosts even if the latter have relatively nearby ($\lesssim 20$ AU) binary companions, thus providing

empirical test of models of terrestrial planet formation in such close binaries (e.g., (20–22)).

Third, when combined with the RV detection of a terrestrial ($m_p \sin i = 1.3 M_\oplus$) planet orbiting very close (0.04 AU) to α CenB (23), which is a solar-type star, it shows that terrestrial planets can form in binaries with diverse properties in terms of host mass and planet-host separation. Although OGLE-2013-BLG-0341LBb was discovered in a search of $\sim 10^3$ microlensing events and α CenBb resulted from intensive observations of a single system, the expected yield in each case (if all stars had similar planets) was roughly unity.

Planets have been discovered in a variety of binary configurations. For example, about 7 transiting circumbinary planets have been discovered in *Kepler* satellite data (24), and two Jovian planets have been found in binary systems using RV (25, 26). Microlensing is also sensitive to planets in very different binary configurations, and both current and future surveys are likely to discover these.

Finally, we discuss an extremely interesting aspect of the modeling of OGLE-2013-BLG-0341 that points to the possibility of much greater sensitivity to systems of this type. When the data near the dip are removed and the remaining lightcurve is fitted for a binary both with and without a planet, the former solution is preferred by $\Delta\chi^2 = 216$ over the no-planet model. That is, although the planet is lighter than the binary by a factor $q < 10^{-4}$, its presence distorts the caustic enough to be noticed in the very high-density observations of the caustic features. Moreover, this model accurately “predicts” the position of the planet. This means that the planet could have been detected even if the source had not passed over the tiny planetary caustic. This passage accounted for $p \sim 1/170$ in the above probability calculation, implying that by probing the central caustic, sensitivity can be improved by $1/p \sim 170$. However, high-density observations (as in Fig. 1) are not routinely taken for binaries. Indeed, μ FUN organized these only because it recognized from the form of the planetary caustic that the source was headed toward the central-caustic region and sought to exploit this passage to obtain information about

the planet. The resultant dense coverage of the binary caustic was inadvertent. Dense followup of “ordinary” binaries may then be the best way to probe for planets in binary systems (27). Because there are a comparable number of high-magnification binary compared to apparently-single-star events, the additional observing resources required to carry out such followup is relatively modest.

Supplementary Materials

www.sciencemag.org

Materials and Methods

Supplementary text

Figs. S1, S2, S3

Table S1

References (28–47)

Supplementary Materials for

A Terrestrial Planet in a ~ 1 AU Orbit Around One Member of a ~ 15 AU Binary

1 Data Collection and Initial Reductions

Data for OGLE-2013-BLG-0341 (RA = 17:52:07.49, Dec = $-29:50:46.0$) (l, b) = (-0.05, -1.68) were obtained through a complex interplay of three modes, real time alerts of ongoing microlensing events, high-cadence monitoring of high magnification events, and intensive monitoring of wide microlensing fields, which appeared historically in that order. The $O(1 \text{ day}^{-1})$ cadences of early surveys were too low to robustly detect and characterize the ~ 1 day planetary perturbations, but since the survey teams using wide-angle cameras were able to detect ongoing events in real time (4), follow-up teams formed to intensively monitor a subset of events using networks of narrow-angle cameras, as suggested by (28). When the OGLE survey upgraded from OGLE-II to OGLE-III, thereby increasing event detection by a factor ~ 10 , it became practical for follow-up teams to focus on rare high-magnification events, which are substantially more sensitive to planets (29). This became the main channel of microlensing planet detection during 2005-2010. See (30) for a thorough review. Further upgrades to OGLE-IV and MOA-II, and the addition of the Wise survey, which all employ very large format cameras, enabled moderately high-cadence ($\gtrsim 1 \text{ hr}^{-1}$) near round-the-clock monitoring of $\gtrsim 10 \text{ deg}^2$ of the densest star fields. This permits planet detection in a much larger number of events without any conscious human intervention (e.g., (31)) thus both greatly increasing the planet detection rate and permitting more rigorous statistical analysis. The introduction of such “second generation” surveys was once thought to eliminate the need for follow-up observations.

Indeed, the binary+planet nature of OGLE-2013-BLG-0341 could have been established

based on survey data alone. Data for the both the “bump” (A) and the “dip” (B) were collected without conscious intervention, and survey data by themselves would have covered the central binary caustic (C–F) well enough to basically characterize it. Nevertheless, by analyzing ongoing OGLE data, which were posted to the web daily, μ FUN detected subtle signs of an approaching caustic and organized intensive observations to capture the entrance (if it occurred). Coordinated efforts of several amateur astronomers in New Zealand, some looking for holes in clouds through which to observe the event, captured this entrance, thereby pinning down the caustic structure much more precisely. This detection then further triggered extremely dense observations, up to $\sim 20 \text{ hr}^{-1}$. It is this extremely dense coverage that permits measurement of such detailed effects as orbital motion and the presence of the planet from central-caustic data alone. See below. In fact, there are several recent events that demonstrate synergy between second-generation surveys and the high-magnification follow-up observations that were previously thought to be a relic of first-generation microlensing (32–34).

The data were reduced using “image subtraction” (aka “difference image analysis”) in which successive images are geometrically and photometrically aligned, convolved to a common point spread function (PSF) and then subtracted from a reference image (35). In principle (and very nearly in practice), this leads to a completely flat “difference image” except where some source has varied, either by changing brightness or by moving between images. The major exception is residuals from bright stars due to imperfect modeling of the PSF. This technique is very important for microlensing observations, which take place in the densest star fields on the sky where it is actually quite rare for a microlensed source not to be blended with a random star along the line of sight. Difference imaging “magically” removes essentially all such irrelevant blends (but see below).

2 Initial Modeling and Re-reductions

Even as OGLE-2013-BLG-0341 was still falling toward baseline, initial models were circulated with the same overall characteristics and similar model parameters to those reported here. It was noted at that time that both close-binary and wide-binary models gave excellent fits to the 2013 data. However, it was then noticed that the wide models “predicted” an earlier passage near the putative wide companion roughly one year earlier. Binning these data revealed a low-amplitude but highly significant “bump” as seen in Fig. 1.

Nevertheless, the early (pre-event) data showed a number of puzzling features that might call into question the reality of this “bump” (and so of the wide-binary interpretation). The OGLE data, which by chance extend back about 15 years into both OGLE-III and OGLE-II, show a steady brightening of about 0.4% per year. Of course, this effect is too small to be seen in individual data points but is plainly visible in binned data. This raised two concerns. First, if the source were variable on long timescales, then it might also have varied on shorter timescales one year before the event, thus giving rise to the “bump”. Second, whatever the origin of this variation, it could affect the estimation of “baseline flux”, which itself is not of any direct interest but can impact other event parameters, which are of interest (e.g., (32)). Hence, a decision was made to wait until the event had effectively returned to baseline to complete the analysis and, in the meantime, to try to track down the origin of the observed long-term variability. An important clue in this regard is that MOA data showed a similar long-term trend and also showed strong variation as a function of position of the source relative to the ground (which changes as functions of time of night and time of year).

We began by consulting variable-star experts who told us flatly that it was extremely unlikely for this type of star (reddish subgiant) to be varying on long timescales at few percent levels.

An intensive investigation revealed that a neighboring star (about 1.5 times the source

brightness and separated from it by $1.3''$) was slowly moving toward the microlensed source at 5 mas yr^{-1} . In the difference images, this star then produced an extremely small dipole “divot”, with an excess flux near the microlensed source and an exactly equal deficit further from it. The excess then entered the tapered aperture used to measure the microlensed source but the deficit did not. As the neighboring star moved closer, the microlensed source appeared to brighten. Detailed modeling showed that this effect completely explained the apparently increasing brightness.

The MOA data have substantially larger PSF than OGLE (due to much better observing conditions in Chile than NZ), meaning that the two sides of the “divot” move in and out of tapered aperture as the PSF varies. This explains the much stronger PSF-effects seen in MOA data, while still accounting for the long term trend. In addition, the larger PSF, together with differential refraction, explains the variations as a function of position relative to the ground. This is seen in many other events and is due simply to the presence of the neighbor, not its motion.

The bottom line is that these effects can be robustly removed from the OGLE data, and can be accounted for in the MOA data. We therefore adjusted the OGLE data to remove this trend, but only used the MOA data within 50 days of the peak, in order to guard against unmodeled effects of neighbor motion in the MOA baseline. Note that we did not check the impact of excluding MOA baseline data, but made the decision solely on the grounds that the corrections were substantially less reliable than for OGLE data.

Rereduced data are available from the corresponding author at the following site.

<http://astroph.chungbuk.ac.kr/~cheongho/OB130341/data.html>

3 Final Modeling

3.1 Event Parameters

Fourteen geometric parameters are required to model the OGLE-2013-BLG-0341 lightcurve, in addition to two flux parameters for each observatory. That is, the observed flux F_i is modeled as $F_i(t) = F_{s,i}A(t) + F_{b,i}$ where $(F_s, F_b)_i$ are the source and blended fluxes at observatory i and $A(t)$ is the (very nearly, see below) observatory-independent magnification.

The overall microlensing event is characterized by the Einstein radius crossing time, t_E , the impact parameter u_0 of the source relative to the host star (designated “primary”) in units of θ_E , and the time t_0 of this approach. The primary’s two companions are each described by their mass ratios (q_2, q_3) and projected separations (s_2, s_3) in units of θ_E relative to the primary. The angle between them is ϕ_{23} , while the angle between the source trajectory and the primary-planet axis is α . Next, $\rho \equiv \theta_*/\theta_E$ where θ_* is the angular source radius. Equivalently, $t_* \equiv \rho t_E$ is the source-radius self-crossing time.

The reflex motion of Earth’s orbit affects the lens-source separation enough to measure the two “microlens parallax” parameters $\boldsymbol{\pi}_E = (\pi_{E,N}, \pi_{E,E})$ (36, 37), whose magnitude is $\pi_E = \pi_{\text{rel}}/\theta_E$, and whose direction is that of the lens-source relative proper motion: $\boldsymbol{\pi}_E/\pi_E = \boldsymbol{\mu}/\mu$. Finally, in many binary and planetary events, it is possible to detect the instantaneous projected orbital motion of the lens components $\boldsymbol{\gamma} = (\gamma_{\parallel}, \gamma_{\perp}) = ((ds/dt)/s, d\psi/dt)$, where ψ is the angular orientation of the binary axis. In hierarchical triples, there could be two such $\boldsymbol{\gamma}$ (although we hold the planet position fixed relative to the host, allowing only binary-star orbital motion).

The microlens parallax and orbital motion is subject to another degeneracy that takes lensing parameters $(u_0, \alpha, \pi_{E,\perp}, \gamma_{\perp}) \rightarrow -(u_0, \alpha, \pi_{E,\perp}, \gamma_{\perp})$, where $\pi_{E,\perp}$ is the component of $\boldsymbol{\pi}_E$ perpendicular to the projected position of the Sun (12, 38). See (38) for a thorough review of this parameterization.

3.2 Modeling Methods

The modeling of the lightcurve is complex and computationally intensive for two interrelated reasons. First, while the majority of the individual data points lie far from the caustics (and so can be evaluated solving a 10th order complex polynomial) or are moderately near (and so solvable using 13 such evaluations in the hexadecapole approximation (39, 40)), there are a very large number of points within or very near the caustics, which must be evaluated using “inverse ray shooting” (41, 42). In this approach, one “shoots” rays back from the observer and calculates where they land on the source plane due to deflections induced by the three bodies. Those landing on the source are weighted by the local surface brightness, which is affected by limb darkening. We use the linear limb-darkening coefficients $u = (0.649, 0.702, 0.754, 0.754)$ (43) for $(I, R/I, R, N)$ filters based on stellar parameters $(T_{\text{eff}}, \log g) = (4250, 3.00)$ found from the source position on the color-magnitude diagram (below), and adopt turbulence of 2 km s^{-1} and solar heavy element abundance (neither of which have any significant effect).

Second, the large number of parameters, together with the presence of sharp features in the lightcurve, can cause “downhill” algorithms to become stuck in false minima.

We therefore organized two completely independent searches of this parameter space by two teams within our collaboration, using two completely independent numerical algorithms. Another collaboration member, not involved in either calculation, then collected the results and led in the resolution of the modest differences.

We label the four solutions Wide (+/-), and Close (+/-). In the wide solutions, the binary companion lies well separated from the host while in the close solution it lies well inside the projected position of the planet. The best fit parameters for each of these four solutions are shown in Table S1. In addition, we show a fifth solution “wide*(-)”, which has the “wide(-)” geometry but for which 144 points in and near the “dip” have been removed from the data. Note that the 3 planet parameters are nearly identical for this solution as the regular “wide(-)”

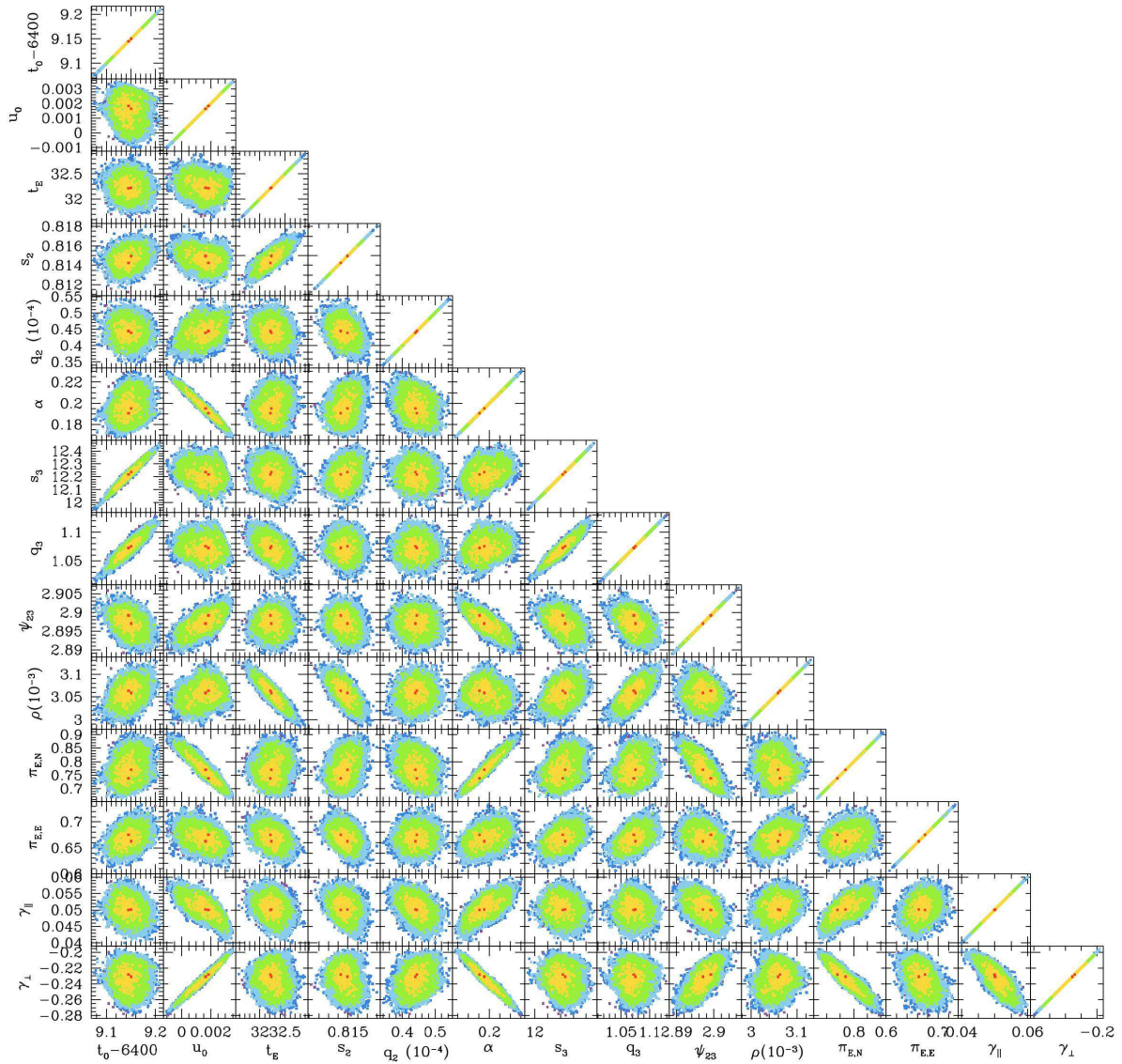


Figure S1: Posterior distribution of 14 microlensing parameters of “wide (plus)” solution, whose central values and errors are shown in Table S1. Color coding indicates points on the Markov Chain within 1 (red), 2 (yellow), 3 (green), 4 (cyan), 5 (blue) sigma of the best fit.

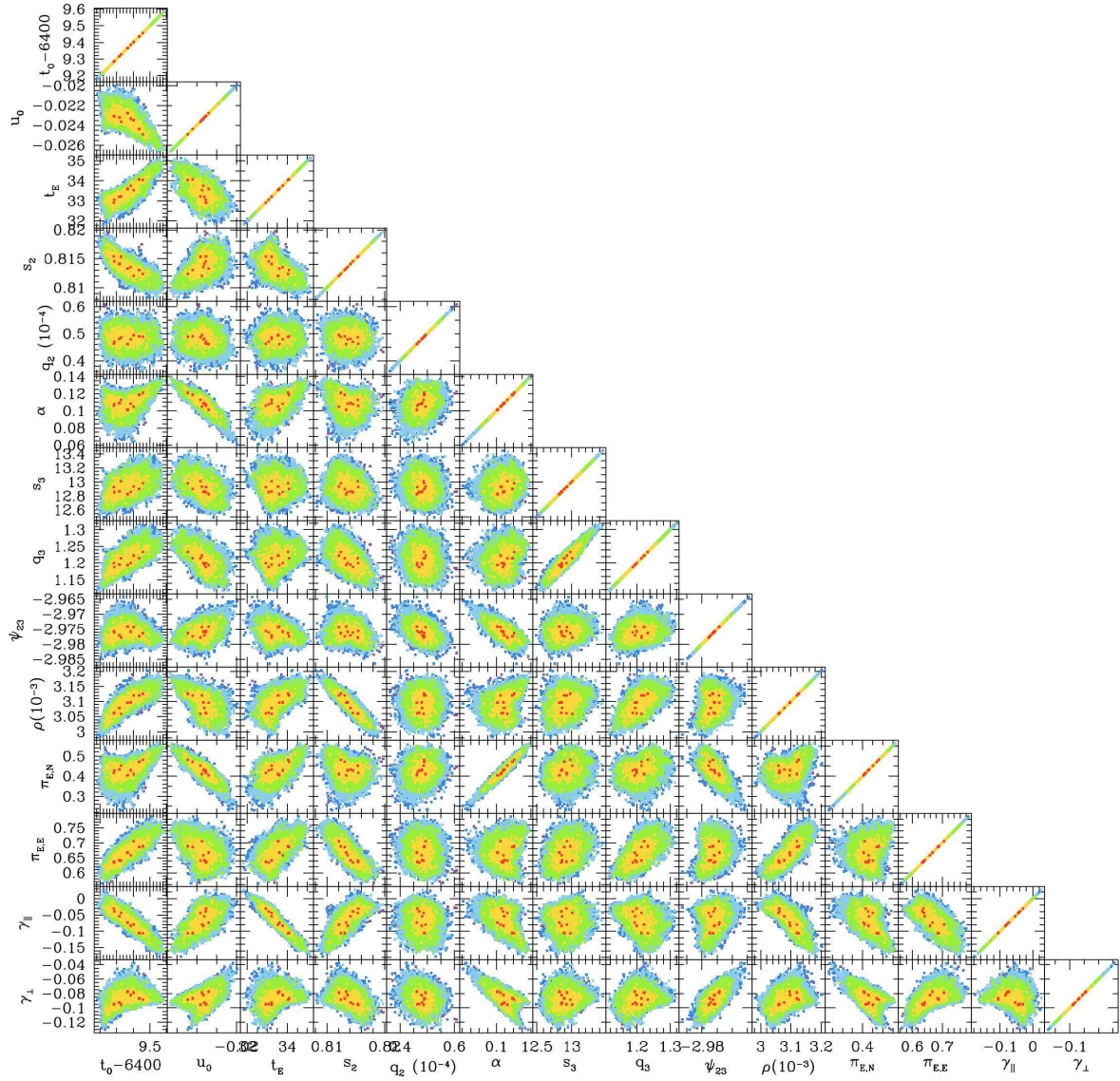


Figure S2: Same as Fig. S1, but for “wide (minus)” solution.

Parameter	Unit	Close(+)	Close(-)	Wide(+)	Wide(-)	Wide*(-)
χ^2/dof		9108 / 8889	9086 / 8889	8876 / 8889	8900 / 8889	8749 / 8755
$t_0 - 6400$	day	2.280 0.049	2.239 0.048	9.148 0.018	9.362 0.078	9.274 0.021
u_0		0.0347 0.0005	-0.0334 0.0004	0.0013 0.0008	-0.0233 0.0010	-0.0238 0.0005
t_E	day	31.40 0.23	31.97 0.23	32.26 0.16	33.41 0.61	32.74 0.08
s_2		0.949 0.002	0.951 0.002	0.815 0.003	0.814 0.007	0.808 0.008
q_2	10^{-4}	1.806 0.157	1.681 0.154	0.443 0.029	0.480 0.033	0.468 0.012
α	radian	-0.0026 0.0028	-0.0065 0.0020	0.1990 0.0106	0.1068 0.0107	0.0871 0.0073
s_3		0.1880 0.0008	0.1863 0.0009	12.2274 0.0334	12.9186 0.0641	13.0299 0.0287
q_3		2.429 0.054	2.420 0.054	1.073 0.015	1.211 0.031	1.215 0.026
ϕ_{23}	radian	0.2765 0.0080	-0.2598 0.0065	2.8967 0.0024	-2.9756 0.0025	-2.9503 0.0089
ρ	10^{-3}	3.1779 0.0274	3.1032 0.0268	3.0543 0.0159	3.0943 0.0276	3.0466 0.0134
$\pi_{E,N}$		-1.740 0.160	1.557 0.141	0.785 0.046	0.421 0.048	0.440 0.015
$\pi_{E,E}$		0.692 0.037	0.981 0.053	0.671 0.016	0.671 0.038	0.631 0.010
γ_{\parallel}	yr^{-1}	2.5944 0.9863	0.7552 1.1885	0.0507 0.0030	-0.0650 0.0346	-0.0200 0.0014
γ_{\perp}	yr^{-1}	1.1523 0.2201	-0.1799 0.1773	-0.2367 0.0150	-0.0852 0.0118	-0.1065 0.0050
I_s		18.5881 0.0088	18.6103 0.0088	18.6130 0.0066	18.6028 0.0111	18.6190 0.0081
$\beta = (E_{\text{kin}}/E_{\text{pot}})_{\perp}$		0.00162 0.00105	0.00033 0.00048	3.70949 0.34936	1.34161 0.41431	1.35543 0.15313

Table S1. OGLE-2013-BLG-0341 microlensing parameters. Best fit values and 1σ error bars for the 14 microlensing model parameters described in Section 3.1, the OGLE source magnitude, and the energy parameter β described in Section 5.2. The first two model columns are “close” binary solutions (both bodies inside the Einstein radius), while the next two show “wide” solutions (one body outside). The “(+/-)” solutions refer to the lens passing on different sides of Earth. The last column shows the best “wide(-)” solution with 144 points near the “dip” removed from the data. It is nearly identical to the “wide(-)” solution with all data.

solution. (s_2, q_2, ϕ_{23}) . This implies that the planet could have been detected and characterized even if the source had missed the planetary caustic (so, no “dip”). Fig. S1 and S2 each show $14 \times 13/2 = 91$ 2-dimensional slices through the posterior distributions of the wide(+) and wide(-) solutions, respectively. Note that these are each well localized relative to the parameter values, except for γ_{\parallel} , whose main interest is that it is near zero (see below). Because of this compactness, the choice of priors plays very little role. We used flat priors.

4 Source Characteristics

In order to measure the Einstein radius $\theta_E = \theta_*/\rho$, one must determine the source radius θ_* . We follow the standard procedure (9). First, we measure the source flux in V (not used in modeling but just for this purpose) and I , which come directly out of the modeling (see above). We then plot the resulting $(V - I, I)_s$ on an instrumental color-magnitude diagram of the field and measure the offset from the centroid of the red giant “clump”. See Fig. S3. If this diagram were calibrated, then the positions of the source and clump would both change, but the offset would not. Next, we use the dereddened color (44) and magnitude (45) of the clump $(V - I, I)_{0,lc} = (1.06, 14.45)$ together with this offset to find the dereddened source $(V - I, I)_{s,0}$. This procedure is known to reproduce the true dereddened color to ± 0.05 (44). We estimate an error in $I_{s,0}$ of ± 0.10 magnitudes based on reproducibility of centroiding the clump. We convert from V/I to V/K using the color-color relations of (46). Finally, we use the empirically determined color/surface-brightness relations of (47) to determine θ_* . We obtain $(V - I)_0 = 1.18 \pm 0.01$ from CTIO data and $(V - I)_0 = 1.15 \pm 0.03$ from OGLE data, and $I_0 = 16.35$, which (after taking account of the above 0.05 and 0.10 errors) yields $\theta_* = 2.89 \pm 0.23 \mu\text{as}$.

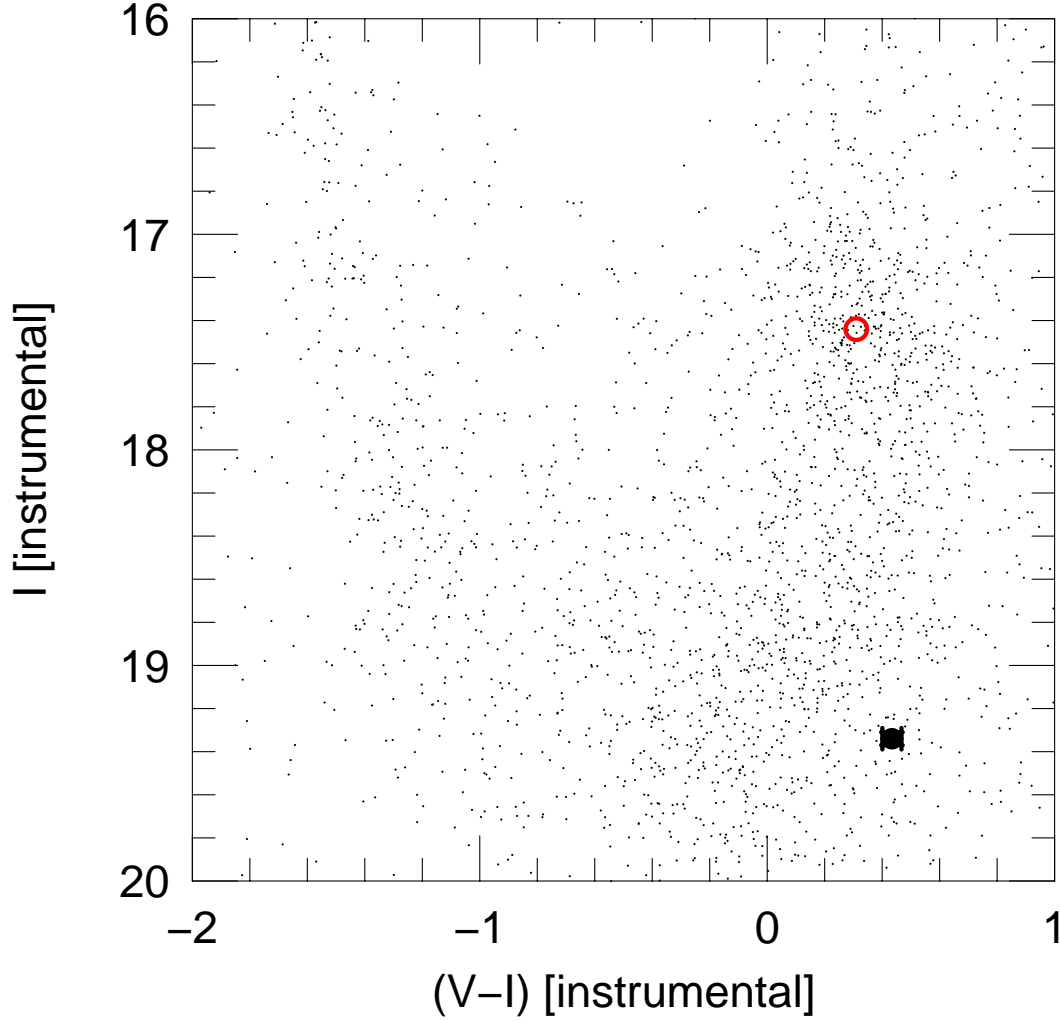


Figure S3: Instrumental CTIO color-magnitude diagram (CMD) showing the position of the OGLE-2013-BLG-0341 baseline source (black) compared to all stars within $90''$. The CMD is deliberately not calibrated because all that is of interest is the difference between the source (black) and the centroid of the red clump (red): $\Delta(V - I, I) = (0.12, 1.90)$. Together with the known position of the clump $(V - I, I)_{0,\text{cl}} = (1.06, 14.45)$, this implies $(V - I, I)_{0,s} = (1.18, 16.35)$. Combined with a similar measurement from OGLE and the color/surface-brightness relation (47), this position implies an angular source radius $\theta_* = 2.89 \pm 0.23 \mu\text{as}$.

5 Higher-Order Effects

There are two higher-order effects that are not obvious from the lightcurve, but have important physical implications: parallax and binary orbital motion.

5.1 Parallax

As illustrated in Fig. 3, if parallax is not included in the model, the residuals are severe: including parallax reduces χ^2 by 730. We now show that, even without detailed modeling, one can infer from the form and amplitude of these residuals that the microlens parallax has amplitude $\pi_E \gtrsim 0.7$. Together with the above determination that $\theta_E \sim 0.9$ mas, this implies (even without detailed modeling) a host mass $M_h = \theta_E / \kappa \pi_E \lesssim 0.15 M_\odot$, planet mass $m_p = q_2 M_h \lesssim 2 M_\oplus$, and distance $D_L = AU / (\theta_E \pi_E + \pi_s) \lesssim 1$ kpc. Detailed modeling then confirms these simple by-eye estimates.

The first point is that microlens parallax is a vector $\boldsymbol{\pi}_E = (\pi_{E,\parallel}, \pi_{E,\perp})$, with the direction being that of the lens-source relative proper motion $\boldsymbol{\mu}$. This is because motion parallel to Earth’s instantaneous acceleration (at the peak of the event) leads to a very different lightcurve distortion than perpendicular motion. For parallel motion, the lens “slows down” during the event, so the rise toward peak is faster than the fall. Hence, (in the approximation of uniform Earth acceleration) there is an anti-symmetric distortion, with the data below the non-parallax model before peak and above after peak. For perpendicular motion, by contrast, the distortion is symmetric. From the point-lens magnification formula (I) $A = (u^2 + 2)(u^4 + 4u^2)^{-1/2}$, one can easily work out that the distortion is given by

$$\frac{\delta A}{A} \simeq 4 \left(\frac{at_E^2}{\text{AU}} \right) G_1(u) \pi_{E,\parallel} - \left(\frac{at_E^2}{\text{AU}} \right)^2 |G_3(u)| \pi_{E,\perp}^2; \quad G_n(u) = \frac{u^n}{(u^2 + 2)(u^2 + 4)}, \quad (3)$$

where a is Earth’s (assumed uniform) acceleration and where we have assumed $u = (t - t_0) / t_E$, i.e., $u_0 \ll 1$. Because the target was at quadrature 35 days before peak, Earth’s acceleration

can be treated as roughly constant during the entire pre-peak interval shown in Fig. 3. Since the second term in Equation (3) is quadratic in π_E and has smaller coefficient, it can usually be ignored to first approximation. Hence, $\delta A/A$ is expected to peak at $u = -0.95$ with a value $\delta A/A = -0.27(at_E^2/\text{AU})\pi_{E,\parallel} \rightarrow 0.087\pi_{E,\parallel}$ where we have used $t_E = 33$ day and $a = (2\pi/\text{yr})^2\text{AU}$. From Fig. 3 the actual peak deviation is $\Delta I = 0.063$ at $u = -0.82$, which corresponds (after accounting for $(F_b/F_s)_{\text{OGLE}} = 0.25$) to $\delta A/A = 0.068$ and hence $\pi_{E,\parallel} = 0.78$. This compares to the model fit of $\pi_{E,E} = 0.67 \pm 0.04$ (noting that Earth’s acceleration is nearly due East at quadrature). Unfortunately, only $\pi_{E,\parallel}$ can be read directly off the lightcurve: $\pi_{E,\perp}$ can only be deduced from detailed modeling. Nevertheless, this estimate of $\pi_{E,\parallel}$ places a lower limit on π_E (hence upper limits on the host mass, planet mass, and distance).

5.2 Binary Orbital Motion

The relative transverse velocity of the two binary components can be measured from two distinct effects. First, the very sharp features and high-density coverage of the central caustic allow detection of subtle changes in the caustic shape and orientation between entrance and exit due to such transverse motion, even though the interval between these caustic passages is only of order a day. For the close binary models, this is the only source of information. For the wide binary models the timing and height of the “bump” give the position of the source relative to the companion roughly 300 days before peak, and this can be compared to the “predicted” position based on the caustic morphology that is measured at peak. The model parameters that capture this effect are the two component vector $\gamma = (\gamma_{\parallel}, \gamma_{\perp})$, which is related to the physical transverse relative velocity $\Delta \mathbf{v}_{\perp} = D_L \theta_E s \gamma$. The measurement of γ can help discriminate between otherwise degenerate models through β , the instantaneous ratio of the projected kinetic energy to the (absolute value of) projected potential energy

$$\beta = \left(\frac{E_{\text{kin}}}{|E_{\text{pot}}|} \right)_{\perp} = \frac{(\Delta v_{\perp})^2 a_{\perp}}{2GM_{\text{tot}}} = \frac{\kappa M_{\odot} \text{yr}^2}{8\pi^2} \frac{\pi_E s^3 \gamma^2}{(1 + q_3) \theta_E (\pi_E + \pi_S / \theta_E)^3}. \quad (4)$$

There are two key points about β . First, if the system is bound, then β must strictly satisfy $\beta < 1$. Second, it is highly improbable (in a sense that we quantify below) that $\beta \ll 1$.

Before discussing these, we note that there must be only two stars (plus planet) giving rise to these phenomena, not three stars (plus planet). Naively one might think that the double-horned peak could be due to a close binary, while the “bump” one year earlier was due to a third star. However, if there were three such stars, their combined effect near peak would not be a simple quadrilateral caustic (See Fig. 2) but a much more complicated self-intersecting caustic, which would cause multiple entrances and exits in the data. The fact that the “double horned peak” is simple shows that there are only two stars.

Next, why must the two stars be bound? That is, why is it not possible that the source has simply passed by two unrelated stars (one with a planet) roughly one year apart? The rate at which any given source is microlensed toward these fields is $\Gamma \sim 10^{-5} \text{ yr}^{-1}$. Hence, the probability for a second encounter, within 1 year and within 3 Einstein radii is 3×10^{-5} . Even if we take a more generous attitude that what is essential is the binary-induced central caustic and so the chance projection of a second star within a $15 \theta_E$ circle (rather than the additional restriction of lying near the source path), a similar calculation yields $p \sim 2 \times 10^{-4}$. This should be compared to the $p > 10\%$ probability that a given star has a binary companion within 15 AU. Hence, this system is very likely to be bound.

We argued in the body of the paper that the system was a wide binary because there was a “bump” in the data very near the time, amplitude and duration predicted by the wide-binary solutions due to the position of the host’s companion in those models. However, there are several “structures” in the baseline data that are due to low-level correlated noise. Such structures are often seen in microlensing data but are ignored because they have no impact on the event analysis. However, because the “bump” plays an important role in the present case, we must take a closer look. As discussed in Section 2, we spent considerable effort tracking down

the apparent long-term brightening of the source. Hence, while it would be very strange if the largest and best defined of these structures happened to basically coincide with the height, width, and time predicted by the wide model, it is still of interest to probe the wide/close degeneracy with independent arguments.

The two close models have $\beta = 0.00162 \pm 0.00105$ and $\beta = 0.00033 \pm 0.00048$. For simplicity of illustration in the following arguments, we choose $\beta = 10^{-3}$. There are three ways in which a binary system can have low β . First, the two components could be in a wide circular orbit but are projected to very close apparent separation. The probability for this viewing angle is $p \sim 2\beta^2 \rightarrow 2 \times 10^{-6}$. Second they could be on circular orbits in which the components happen to be traveling directly along our line of sight (or very close to it). The probability for this is again $p \sim 2\beta^2 \rightarrow 2 \times 10^{-6}$. Third, they could be observed near apocenter in face-on highly eccentric orbits. The required eccentricity is then $e \simeq 1 - \beta/2 = 0.9995$. First, there are no binaries observed in nature with eccentricities anywhere near this value. But even if this were one of the few such systems, it would have a pericenter $q \sim a_{\perp}\beta/4 < 0.1R_{\odot}$ which is not physically possible. Of course, one could imagine combinations of these possibilities. For example, if we chose a more reasonable eccentricity of $e = 0.9$, then the pericenter would be physically allowed, and the required viewing angle less restrictive, but still $p \sim 10^{-5}$. Hence, very low β is highly improbable to the point of being ruled out.

The two wide solutions both have central values $\beta > 1$, which would be unphysical. For the wide(-) solution, β is within 1σ of being physically allowed and within 2σ of having a “typical” value. On the other hand, the wide(+) solution is formally favored by $\Delta\chi^2 = 24$. This proves that there are systematic errors at the level of $\Delta\chi^2 \sim 20$, which is not surprising given the level of correlated noise at baseline and also given experience with previous microlensing events. That is, we can be confident that a “bump” is detected ~ 300 days before the main peak, but we are cautious about deriving detailed parameters based on the morphology of this bump, which

is visible only in binned data. Therefore, we consider both the wide(+) and wide(-) solutions to be acceptable. Since these represent similar physical systems, this ambiguity does not impact our conclusions.

We note that for many events, the parallax and orbital motion parameters are correlated, and in particular $\pi_{E,\perp}$ can be highly correlated with γ_{\perp} (38) because these two parameters induce similar distortions on the wings of the lightcurve. However, this is not an issue in the present case because while the parallax signal does indeed come from the wings of the lightcurve (see Fig. 3), the orbital motion parameters are determined from the location and height of the “bump”, which occurred well within the “baseline” region of the lightcurve, long before the onset of the rising wing.

References and Notes

1. A. Einstein, *Science* **84**, 506 (1936).
2. G. M. Kennedy, S. J. Kenyon, *Astrophys. J.* **673**, 502 (2008).
3. B. S. Gaudi, *ARA&A* **50**, 411 (2012).
4. A. Udalski, *Acta Astron.* **53**, 291 (2003).
5. I. A. Bond et al., *Mon. Not. R. Astron. Soc.* **327**, 868 (2001).
6. T. Sumi et al., *Astrophys. J.* **591**, 204 (2003).
7. Y. Shvartzvald, D. Maoz, *Mon. Not. R. Astron. Soc.* **491**, 3631 (2012).
8. Supplementary Materials (this work).
9. J. Yoo et al., *Astrophys. J.* **603**, 139 (2004).

10. A. Gould, N. Andronov, *Astrophys. J.* **516**, 236 (1999).
11. A. Gould, K. Horne, *Astrophys. J.* **779**, 28 (2013).
12. M. Smith, S. Mao, B. Paczyński, *Mon. Not. R. Astron. Soc.* **339**, 925 (2003).
13. W. Zhu et al., *Astrophys. J.* in press (2014) arXiv:1403.4936.
14. M. Mayor et al., *Astron. Astrophys.* submitted arXiv:1109.2497.
15. S. Dong, Z. Zhu, *Astrophys. J.* **778**, 53.
16. E. Petigura, A. W. Howard, G. W. Marcy, *PNAS* 11019652.
17. J. J. Swift et al., *Astrophys. J.* **764**, 105 (2013).
18. C. D. Dressing, D. Charbonneau, *Astrophys. J.* **767**, 95 (2013).
19. A. Cassan et al., *Nature* **481**, 167 (2012).
20. M. Barbieri, F. Marzari, H. Scholl, *Astron. Astrophys.* **396**, 219 (2002).
21. E. V. Quintana et al., *Astrophys. J.* **660**, 807 (2007).
22. R. R. Rafikov, *Astrophys. J.* **765**, L8 (2013).
23. X. Dumusque et al., *Nature* **491**, 207 (2012).
24. W. F. Welsh et al., *Nature* **481**, 475 (2012).
25. A. P. Hatzes et al., *Astrophys. J.* **599**, 1383 (2003).
26. S. Zucker et al., *Astron. Astrophys.* **426**, 695 (2004).
27. D.-W. Lee et al., *Astrophys. J.* **672**, 623L (2008).

28. A. Gould, A. Loeb, *Astrophys. J.* **392**, 104 (1992).
29. K. Griest, N. Safizadeh, *Astrophys. J.* **500**, 37 (1998).
30. A. Gould et al., *Astrophys. J.* **720**, 1073 (2010).
31. R. Poleski et al., *Astrophys. J.* **782**, 47 (2014).
32. J. C. Yee et al., *Astrophys. J.* **755**, 102 (2012).
33. C. Han et al., *Astrophys. J.* **762**, L28 (2013).
34. J. C. Yee et al., *Astrophys. J.* submitted arXiv1403.2134 (2014).
35. C. Alard, R. Lupton, *Astrophys. J.* **503**, 325 (1998).
36. A. Gould, *Astrophys. J.* **392**, 442 (1992).
37. A. Gould, *Astrophys. J.* **606**, 319 (2004).
38. J. Skowron et al., *Astrophys. J.* **606**, 319 (2011).
39. O. Pejcha, D. Heyrovský, *Astrophys. J.* **690**, 1772 (2009).
40. A. Gould, *Astrophys. J.* **681**, 1593 (2008).
41. P. Schneider, A. Weiss, *Astron. Astrophys.* **164**, 237 (1986).
42. P. Schneider, A. Weiss, *Astron. Astrophys.* **171**, 49 (1987).
43. A. Claret, *Astron. Astrophys.* **363**, 1081 (2000).
44. T. Bensby et al., *Astron. Astrophys.* **549A**, 147 (2013).
45. D. Nataf et al., *Astrophys. J.* **769**, 88 (2013).

46. M. S. Bessell, J. M. Brett, *PASP* **100**, 1134 (1988).

47. P. Kervella et al., *Astron. Astrophys.* **426**, 297 (2004).

Acknowledgments: We acknowledge: NSF AST-1103471 (AG,BSG,JCY); NASA NNGX12AB99G (AG,BSG,RWP); OSU Fellow and NASA Sagan Fellow (JCY); ERC AdG 246678, IDEAS program (AU); Polish MNiSW IP2011026771 (SK); Korea NRF CRIP 2009-0081561 (CH); US-Israel BSF(AG,DM); JSPS23340044, JSPS24253004 (TS); NZ Marsden Fund (PCYK); Israel SF PBC-ICORE 1829/12 (DM); NSF grant AST-1211875 (DB). Data available at <http://astroph.chungbuk.ac.kr/~cheongho/OB130341/data.html>